UCLA

UCLA Electronic Theses and Dissertations

Title

Analysis of a Micro-scale, Tri-axial, Capacitive-based, Differential Force Sensor for Haptic Feedback System in Robotic Surgery

Permalink

https://escholarship.org/uc/item/8zz2q7qw

Author

Mancillas, Francisco Javier

Publication Date

2018

Peer reviewed|Thesis/dissertation

UNIVERSITY OF CALIFORNIA

Los Angeles

Analysis of a Micro-scale, Tri-axial, Capacitive-based, Differential Force Sensor

for Haptic Feedback System in Robotic Surgery

A thesis submitted in partial satisfaction

of the requirements for the degree Master of Science

in Electrical Engineering

by

Francisco Javier Mancillas

2018

ABSTRACT OF THE THESIS

Analysis of a Micro-scale, Tri-axial, Capacitive-based, Differential Force Sensor

for Haptic Feedback System in Robotic Surgery

by

Francisco Javier Mancillas

Master of Science in Electrical Engineering

University of California, Los Angeles, 2018

Professor Robert N. Candler, Chair

It is known that the absence of tactile feedback in robotic surgery represents a limiting factor to surgeons. In effect, the lack of tactile feedback in robotic surgical tools is closely associated with tissue damage. This is especially true among novice surgeons who, not having surgical tools that measure compressive sensing, apply excessive force causing tissue crush injuries. Additionally, the lack of tactile feedback in the shear directions lead to additional problems, such as breaking of sutures due to excessive pull forces. In view of the lack of tactile feedback, our efforts have been focused on developing a highly sensitive micro-scale, tri-axial, capacitive-based, differential force sensor. To this end, we provide relevant derivations to single-element, multi-axis capacitive sensing including an illustrative discussion on capacitive pressure sensor (CPS) theory. We begin our discussion on CPS theory with the well-known parallel plate capacitor to illustrate key physical concepts and move on to more complex structures, such as capacitors with

asymmetrical surface areas under deformation. Whenever possible, we provide explicit capacitance expressions for these last structures and demonstrate that such expressions reduce to more familiar ones. To ensure the validity of our theoretical calculations, we have also provided results obtained from COMSOL Multiphysics simulations. It is worth mentioning that for our theoretical calculations, we have only considered deformations in the downward direction as a result of external forces applied to the top surface of the CPS model so as to facilitate the evaluation of capacitance expressions. For the COMSOL Multiphysics simulations of our proposed capacitive force sensor (CFS) model, on the other hand, no restrictions are imposed on the direction of deformation. The design, including sensor location and performance criteria, of our current CFS model is also considered as well as its working principle.

The thesis of Francisco Javier Mancillas is approved.

Kang Lung Wang

Chee Wei Wong

Robert N. Candler, Committee Chair

University of California, Los Angeles

2018

To YHWH Elohim. Infinitely, thank you.

TABLE OF CONTENTS

ACKNOWLEDGMENTS

To my family, thank you for all your unconditional support in all my decisions. I am forever thankful to you all. You are part of my academic success.

To all the members of the Sensors and Technology Lab, my colleagues, thank you so much for all your help and support during the MS Thesis Program at UCLA.

Professor Candler, words are not enough to express my most sincere gratitude for allowing the opportunity to be part of your research group. I would also like to thank you for all your guidance and patience.

To the members of the committee: Dr. Chee Wei Wong and Dr. Kang Wang, thank you so much for all your advice and words of encouragement. It was a true honor and delight learning from both of you inside and outside of classroom.

CHAPTER 1 INTRODUCTION

Minimally invasive surgery (MIS) is characterized by operational procedures in which surgeons make small incisions in the skin, typically a few millimeters. Due to the size of these incisions, patients tend to recover quickly and experience less discomfort than with conventional surgery. The many benefits and advantages that MIS offers over traditional open surgery have ultimately lead MIS to become more and more predominant in hospitals. MIS, however, requires a high level of dexterity and great precision of laparoscopic instruments, both of which are not easily achieved by the novice surgeon, and, as a result, only a limited number of qualified candidates can perform such operations. Not to mention that not all procedures can be done through minimally invasive methods. Although it is undeniable that MIS offers great advantages to the patient, it has also introduced new surgical challenges. For example, the introduction of laparoscopic tools into MIS has inadvertently introduced the loss of tactile information from inside a patient's body to the surgeon's fingertips. As such, the lack of touch sensation could potentially lead to undesirable patient's complications due to excessive forces being applied to tissues.

1.1 History and Predictions of Minimally Invasive Surgery

In 1901, the first experimental laparoscopy was performed in an animal model. A German surgeon, George Kelling, made a small incision in the abdomen of dogs, insufflated the peritoneal cavity with sterile air, and investigated the abdomen with a cystoscope. He created the term *coelioskope* for his visionary procedure. Although his work found little support, his research established the importance of a sterile pneumoperitoneum to allow visualization, an anchoring principle for future laparoscopy. Near the time of Kelling's animal experiments, the seeds of minimally invasive techniques in humans were being planted. Hans Christian Jacobaeus, an

internist in Stockholm, introduced the term *laparothorakoskopie* in his unprecedented report on laparoscopy and thoracoscopy in humans. This seminal paper was published in *Münchener Medizinische Wochenschrift* in 1911. Interestingly, in this paper, Jacobaeus reported thoracoscopy as a more promising procedure than laparoscopy [1].

Over the next several decades, improvements to the techniques and instruments increased the popularity of laparoscopy. However, it was not until after the first laparoscopic cholecystectomy (LC) was reported in 1987 by Philippe Mouret in Lyon, France, that the revolution in minimally invasive surgery began. This was in large part due to the introduction of a real-time, high-resolution video camera that could be attached to the endoscope and allowed a clear magnified image of the entire operating field to be shown on a monitor [1], not to mention the shorter recovery times experienced by patients. Today, minimally invasive surgery constitutes nearly six percent of the 51 million procedures nationally [2], including 1 million laparoscopic cholecystectomies.

Although the number of common surgeries already performed laparoscopically is expected to continue growing, the current marker for minimally invasive surgery necessitates advances in technology. Specifically, the surgical volume must be large enough for investments to be made to improve the current technology and modify existing equipment. Future projections show that for the majority of common surgeries already performed laparoscopically, the number will grow in the coming years according to a study done in 2011 [3]. The date obtained from this study, along with the 5- and 10-year projections, also suggest that minimally invasive techniques have and will continue to be a viable option and a significant part of the future of healthcare [4].

1.2 Robotic Surgery

Robotic surgery is a type of minimally invasive surgery which utilizes miniaturized surgical instruments and ultimately allow surgeons to perform delicate surgical procedures. It comes as no surprise, therefore, that more and more top surgeons are choosing to perform surgery with the help of robotic tools. One of these tools is the da Vinci Surgical Robot that allows doctors to operate with greater precision and minimal discomfort for the patient. These systems also offer great advantages over traditional laparoscopic surgery, including three additional degrees of motion, tremor removal, and elimination of the fulcrum effect—the consequence of manipulating internal tissues and organs with laparoscopic instruments outside the body. One major drawback of robotic surgery is that the commercially available robotic surgical systems of today are lacking tactile feedback and evidence suggests that a lack of feedback can lead to excessive grip forces, tissue crush injuries, and ruptured sutures [5].

Surgical robots first appeared in 1985, when Kwoh et al. leveraged an industrial programmable universal manipulation arm (PUMA 560) for a neurobiopsy application [6]. Indisputably, robotic surgery platforms provide the same benefits as traditional minimally invasive surgery, including smaller incisions, shorter recovery times, lower risk of infection, and reduced pain as compared to open surgery. Furthermore, robotics are expected to impact the field of minimally invasive surgery as the use of robotics or *computer assistance* enhances the performance of complex procedures, such as elimination of hand tremor, dexterity enhancement, motion scaling and 3D visualization [7]. While the adoption of robotic surgical tools accelerates nationwide [3], these systems are characterized by an absence of touch sensation, which ultimately impedes transition of more delicate procedures. Likewise, excessive grip forces could induce tissue damage, including scar formation, hemorrhaging, perforations, and adhesions [8].

3

Furthermore, without tactile information, surgeons require additional training to reach proficiency on the available surgical robots [9]. Although robotics addresses a subset of surgical procedures, efforts to develop and integrate biocompatible sensor arrays with commercial robotic surgical systems remain inadequate. The development of innovative sensing technologies capable of restoring touch sensation is therefore critical. Several researchers have already proposed solutions to incorporate force feedback into current laparoscopic tools. Many of these solutions involve adding force sensors, such as strain gauges, to record forces at the tool tip or developing a new robotic manipulator used to operate laparoscopic tools and obtain force feedback. Additional work has been done in creating new laparoscopic tools with force feedback incorporated into their designs. However, there still exist many problems within the designs of laparoscopic tools and their use in robotic surgery [10].

1.3 Benefits of Minimally Invasive Surgery

By using minimally invasive surgery techniques, surgeons can offer patients many benefits over traditional surgeries. Among the most prominent benefits, we find the following [11]:

1. **Less Pain**: MIS procedures cause less post-operative pain and discomfort. Studies have shown that patients undergoing MIS procedures report less pain and require smaller doses of pain relievers than patients undergoing traditional surgeries.

2. **Shorter Hospital Stay**: shorter hospital stay and quicker return to normal activities. Patients who undergo MIS procedures are usually able to go home sooner. And, in many cases, the patient is able to return to normal activities and work more quickly.

3. **Less Scarring**: MIS procedures require smaller incisions -- which means smaller, less noticeable scars. The scars that do form as a result of MIS typically have a less jagged edge -- giving them a more appealing look.

4. **Less Injury to Tissue**: most traditional surgeries require a long incision. This incision usually has to be made through muscle. Muscle needs a significant time to heal after surgery. Because there are no long incisions in MIS, surgeons often do not have to cut through muscles to complete the procedure -- leading to less tissue damage and quicker recovery.

5. **Higher Accuracy Rate**: a higher accuracy rate for most procedures. Because MIS procedures use video-assisted equipment, the surgeon has better visualization and magnification of internal organs and structure. For patients, this translates into a more accurate and definitive procedure.

For comparison purposes, we have included Table 1.3 which summarizes the pros and cons of minimally invasive surgery and traditional open Surgery. It is worth pointing out that the main disadvantage of all MIS is the *lack of tactile feedback*. In effect, independent studies have shown that traditional laparoscopic surgery and robotic-assisted laparoscopic surgery, without tactile feedback, can lead to higher prevalence of suture rupture and premature suture failure, both intra- and postoperatively. Therefore, one can conclude that the addition of tactile feedback to laparoscopic and robotic laparoscopic systems can reduce intraoperative complications and result in improved patient outcomes [4].

Table 1.3 Comparison between MIS and traditional open surgery

|	Laparoscopic (MIS)	Robotic (MIS)	Open
Advantages	Minimal Scarring Reduced trauma Shorter recovery time	All benefits of MIS Tremor removal 3D vision Scaled movements	Direct patient contact Surgeon familiarity Availability
Disadvantages	Diminished tactile feedback No 3D vision Poor dexterity	Absence of tactile feedback Longer surgeries Expensive tooling	Long recovery periods Scar formation Painful

CHAPTER 2 CAPACITIVE PRESSURE SENSOR THEORY

2.1 Capacitance of a Parallel Plate Capacitor

We begin our discussion on capacitive pressure sensor theory with the simplest capacitor model that will serve us to illustrate key physical concepts. Namely, a capacitor formed from a pair of parallel plates such as the one shown in Figure 2.1.1. In this configuration, each plate is connected to one terminal of a battery, which acts as a source of potential difference. If the capacitor is initially uncharged, the battery establishes an electric field in the connecting wires when the connections are made. This electric field in the wires causes electrons to migrate in opposite direction of the electric field, e.g. the terminal of the battery, until the plate (now negatively charged), the wire, and the terminal are all at the same electric potential. Once electrostatic equilibrium is achieved, a potential difference no longer exists between the terminal and the plate, and as a result no electric field is present in the wire, and the migration of electrons ceases. The plate now carries an excess negative charge $-Q$, while the other plate has a deficit of

electrons caused by the migration of electrons, leaving this last plate positively charged $+Q$. In this final configuration, the potential difference across the capacitor plates is the same as that between the terminals of the battery.

Figure 2.1.1 A capacitor consists of two conductors, a positive and negative electrodes or plates, so that when it is charged, the conductors carry charges of equal magnitude and opposite sign. As a result, we can describe a capacitor as a device that stores charge and therefore energy. Image from *Physics for Scientists and Engineers with Modern Physics*.
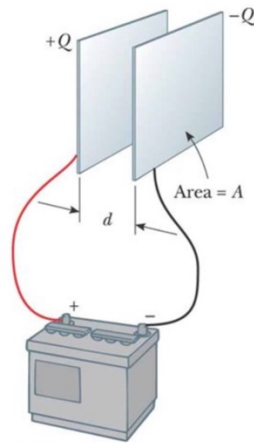
Let us compute the capacitance of a parallel plate capacitor by considering two parallel metallic plates of equal area A are separated by a distance d as shown in Figure 2.1.1. Once steady state conditions are met, one plate carries a negative charge $-Q$ while the other carries a positive charge $+Q$. We would then expect the capacitance of such configuration to increase as the plate area is increased. This is because the larger the plate area, the larger the amount of charge that can be stored on the plate for a given potential difference. We may also arrive at the same conclusion by considering the definition of capacitance, which is defined as the amount of charge Q can be stored per unit volt or potential difference ΔV,

$$C = \frac{Q}{\Delta V} \qquad (2.1.1)$$

where ΔV is defined as the change in potential energy ΔU of the system when a test charge q_0 is moved between two points divided by the test charge, $\Delta V = \Delta U / q_0$. An explicit mathematical expression for the potential difference between points A and B in an electric field $\boldsymbol{E}$ is given by the line integral

$$\Delta V = V_B - V_A = -\int_A^B \boldsymbol{E} \cdot d\boldsymbol{s} \tag{2.1.2}$$

Now, by assuming the accumulated charges are capable of distributing themselves evenly over the entire plate area so that the surface charge density σ becomes constant, $\sigma = Q/A$, we find that

$$C = \frac{Q}{\Delta V} = \frac{A\sigma}{\Delta V} \tag{2.1.3}$$

Thus, from Equation 2.1.3, we can clearly see that the capacitance increases as the plate area increases. Let us focus on another parameter of importance, namely, the distance d that separates the plates. If the battery has a constant potential difference between its terminals, then the electric field between the plates must increase as d is decreased so that the line integral remains constant. On the other hand, if the electric field is constant, then decreasing the distance d also decreases the magnitude of the potential difference ΔV. As a result, we expect the capacitance of the pair of plates to be inversely proportional to d. Having stated the above physical arguments, we proceed with our derivation as follows:

1. Assume that the electric field $\boldsymbol{E}$ between the plates is approximately constant as shown in Figure 2.1.3. This assumption is typically valid, as we will show later, provided that $d \ll \sqrt{A}$. This last condition is, more often than not, erroneously cited by many authors as the distance between the plates being much less than either side of the capacitor, which is

certainly valid only for a square capacitor. Provided the electric field is constant, then, the potential difference becomes

$$\Delta V = V_B - V_A = Ed \tag{2.1.4}$$

2. Assume the surface charge density σ on either plate is constant with magnitude Q/A. Then, using Gausses' Law, we find that the electric field is given by

$$E = \frac{\sigma}{\epsilon} = \frac{Q}{\epsilon A} \tag{2.1.5}$$

where $\epsilon = \epsilon_r \epsilon_0$. Here, ϵ_r is the relative permittivity of the dielectric material between the plates and ϵ_0 is the permittivity of free space and is approximately equal to 8.854×10^{-12} F/m.

3. Substituting the expression for the electric field from Equation 2.1.5 into Equation 2.1.4, and this last one into Equation 2.1.1, we find that

$$C = \frac{Q}{\Delta V} = \frac{Q}{\left(\frac{Qd}{\epsilon A}\right)}$$

$$C = \frac{\epsilon A}{d} \tag{2.1.6}$$

Therefore, the capacitance of a parallel-plate capacitor is proportional to the area of its plates and inversely proportional to the plate separation, just as we had anticipated from our conceptual argument.

9

Figure 2.1.2 [12] The electric field E between the plates of a parallel-plate capacitor is uniform near the center but non-uniform near the edges. Such end effects can be neglected if the plate separation is small compared with the square root of the area of the plates. Note that the electric field lines (labeled →) originate at the positive terminal and terminate at the negative one.
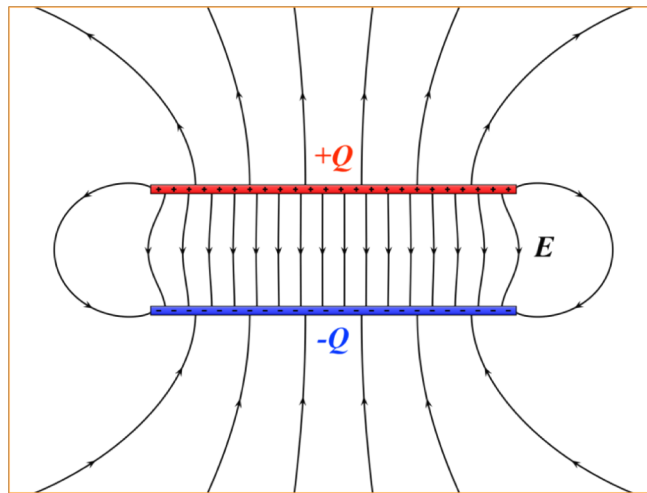
2.2 Capacitance of a Parallel Plate Capacitor with Asymmetrical Surface Area

In this section, we begin our discussion with the most general equation of the electric potential V for a charged plate with infinitely small thickness. For convenience, we express such equation for V in a suitable form that will be useful in section 2.4 once deformations of the plates are introduced. Having expressed V as a surface integral, we subsequently obtain an expression for the potential difference ΔV between two parallel plates, which ultimately allows us to compute the capacitance of a parallel plate capacitor with asymmetrical surface area. That is, a capacitor characterized by having dissimilar surface areas for its electrodes and commonly referred to as asymmetrical capacitor. We finally prove, towards the end of this section, that the capacitance of an asymmetrical square capacitor reduces to the classical capacitance of a parallel plate capacitor, Equation 2.1.6, for a symmetrical square capacitor to ensure the validity of our theoretical results.

In section 2.1, we defined the potential difference ΔV as the change in potential energy divided by the charge q_0 of the test charge. It is customary to set the electric potential to zero ($V_A = 0$) at infinity ($r_A = \infty$) so that the potential difference becomes

$$\Delta V = -\int_A^B \boldsymbol{E} \cdot d\boldsymbol{s} = -\int_A^B k_e \frac{q}{r^2}\hat{\boldsymbol{r}} \cdot d\boldsymbol{s} = -\int_A^B k_e \frac{q}{r^2}cos\theta ds$$

$$\Delta V = -\int_{r_A}^{r_B} k_e \frac{q}{r^2} dr = k_e q \left[\frac{1}{r_B} - \frac{1}{r_A}\right] = k_e q \frac{1}{r_B}$$

where k_e is Coulomb's constant and $\hat{\boldsymbol{r}}$ is a unit vector in the direction of the electric field. With this reference choice, the electric potential created by a point charge at any distance r from the charge reduces to

$$V = k_e \frac{q}{r} \tag{2.2.1}$$

Now, let us suppose there is continuous charge distribution such as the one shown in Figure 2.2.1. If we break up such configuration into elements of charge Δq, we may evoke the superposition principle to compute the total electric potential V at point P for finite point charges

$$V = k_e \sum_i \frac{q_i}{r_i} \tag{2.2.2}$$

As Δq becomes infinitesimally small, the above Riemann sum becomes an integral

$$V = \lim_{n \to \infty} k_e \sum_{i=1}^{n} \frac{\Delta q}{r_i} = k_e \int \frac{dq}{r} \tag{2.2.3}$$

11

Figure 2.2.1 The electric potential at the point P due to a continuous charge distribution can be computed by dividing the charge distribution into elements of charge dq and summing the electric potential contributions over all elements. The color map is used to represent all surface area patches of charge dq at the same height z.
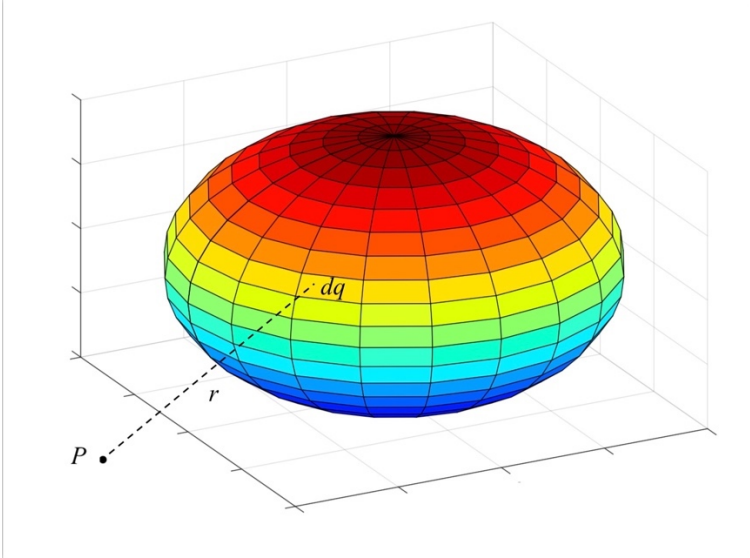
Using Equation 2.2.3, we therefore find that the electric potential V at the point P (x_0, y_0, z_0) of a

charged plate with infinitely small thickness and surface charge density $\sigma = dq/dS$ such as the

one shown in Figure 2.2.2 is given by the surface integral

$$V(x_0, y_0, z_0) = k_e \iint\limits_S \frac{\sigma dS}{[(x - x_0)^2 + (y - y_0)^2 + (z - z_0)^2]^{1/2}} \qquad (2.2.4)$$

Figure 2.2.2 Deformed charged plate with infinitesimal thickness and surface S. The region D is the projection of the surface S into the xy-plane. In this case, such projection is a rectangle, but it might not be the case for other surfaces.
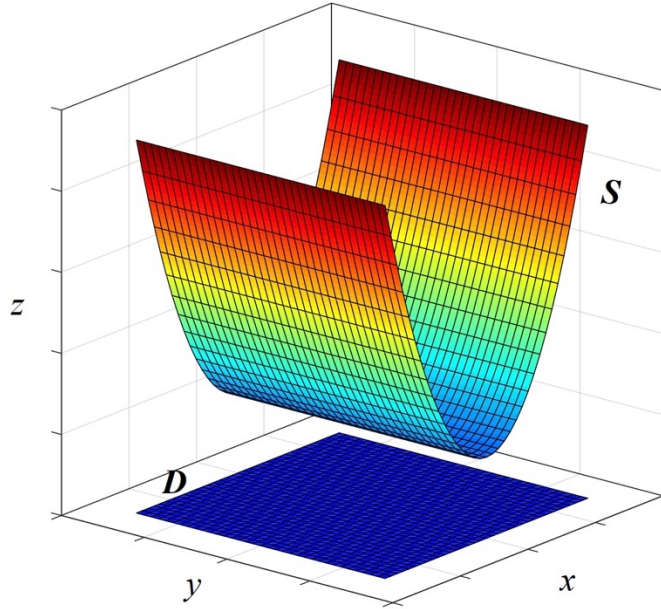
For reasons that will become clear in Section 2.4, it is convenient to transform the surface integral Equation 2.2.4 into a more suitable form

$$V(x_0, y_0, z_0) = \iint\limits_{D} f(x, y, g(x, y)) \sqrt{1 + \left(\frac{\partial g}{\partial x}\right)^2 + \left(\frac{\partial g}{\partial y}\right)^2} \, dA \qquad (2.2.5)$$

where $z = g(x, y)$ describes the surface S in which the charge resides and $f(x, y, g(x, y)) \equiv k_e \sigma / [(x - x_0)^2 + (y - y_0)^2 + (g(x, y) - z_0)^2]^{1/2}$. For a *flat* parallel plate, $g(x, y)$ is constant, and, as a result, its partial derivatives with respect to x and y vanish. Therefore, the electric potential for a flat parallel plate reduces to

13

$$V(x_0, y_0, z_0) = \iint\limits_{D} f(x, y, g(x, y)) \, dA$$

$$V(x_0, y_0, z_0) = k_e \iint\limits_{D} \frac{\sigma dy dx}{[(x - x_0)^2 + (y - y_0)^2 + (g(x, y) - z_0)^2]^{\frac{1}{2}}} \qquad (2.2.6)$$

We are now in the position to compute the potential difference ΔV between two flat parallel plates of unequal surface areas. Such charge system is illustrated in Figure 2.2.3. To facilitate the amount of computation, we let the top plate be located at $z = z_0$ so that $g(x, y) = z_0$. Similarly, we let the bottom plate be at $z = 0$ so that $g(x, y) = 0$. Then, the potential difference of the charge system at the points $P_1(x_0, y_0, z_0)$ and $P_2(x_0, y_0, 0)$ is given by

$$\Delta V = V_+ - V_- = V[P_1(x_0, y_0, z_0)] - V[P_2(x_0, y_0, 0)] \qquad (2.2.7)$$

where

$$V_+ = k_e \left[\iint\limits_{D_1} \frac{\sigma_1 dy dx}{[(x - x_0)^2 + (y - y_0)^2]^{\frac{1}{2}}} + \iint\limits_{D_2} \frac{\sigma_2 dy dx}{[(x - x_0)^2 + (y - y_0)^2 + z_0^2]^{\frac{1}{2}}} \right]$$

$$V_- = k_e \left[\iint\limits_{D_1} \frac{\sigma_1 dy dx}{[(x - x_0)^2 + (y - y_0)^2 + z_0^2]^{\frac{1}{2}}} + \iint\limits_{D_2} \frac{\sigma_2 dy dx}{[(x - x_0)^2 + (y - y_0)^2]^{\frac{1}{2}}} \right]$$

14

Figure 2.2.3 Charge system of two flat parallel plats of dissimilar surface areas. In this case, the top plate consists of charge $+Q$ and surface charge density $\sigma_1 = dQ_1/dS_1$; the bottom plate, on the other hand, of $-Q$ and surface charge density $\sigma_2 = dQ_2/dS_2$. Note that plates' projections into the xy-plane (not shown) are D_1 and D_2 for the top and bottom plates, respectively.
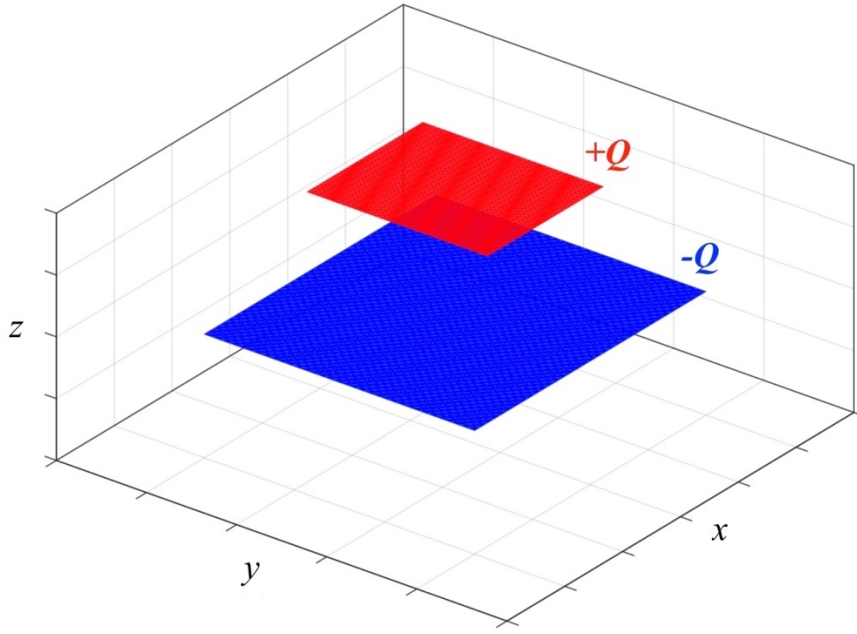
Combining like terms, we obtain

$$\Delta V = k_e \left[\iint_{D_1} \left\{ \frac{1}{[(x-x_0)^2 + (y-y_0)^2]^{\frac{1}{2}}} - \frac{1}{[(x-x_0)^2 + (y-y_0)^2 + z_0{}^2]^{\frac{1}{2}}} \right\} \sigma_1 dy dx \right] -$$

$$k_e \left[\iint_{D_2} \left\{ \frac{1}{[(x-x_0)^2 + (y-y_0)^2]^{\frac{1}{2}}} - \frac{1}{[(x-x_0)^2 + (y-y_0)^2 + z_0{}^2]^{\frac{1}{2}}} \right\} \sigma_2 dy dx \right] \quad (2.2.8)$$

Typically, σ is a function of position because as the capacitor is being charged, the charges have to distribute themselves over the entire plate's surface area. Thus, we would expect a higher density of charge near the center of the plate as the capacitor is being charged, assuming the connection of the plate with the wire is located at the center of the capacitor, of course. Under

steady state conditions, however, we would expect the charges to distribute themselves evenly over the entire area, resulting in constant surface charge density. Therefore, if we assume that the surfaces charge densities are indeed constant and evoke the charge neutrality condition, Equation 2.2.8 can be further simplified. The charge neutrality condition and the assumption of constant surface charge densities for the plates are summarized as follows

$$\left.\begin{aligned} Q_1 + Q_2 &= 0 \\ \frac{Q_1}{A_1} &= \sigma_1 \\ \frac{Q_2}{A_2} &= \sigma_2 \end{aligned}\right\}$$

(2.2.9)

Solving for σ_2 in terms of σ_1, we find that $\sigma_2 = -\sigma_1(A_1/A_2)$. Thus, Equation 2.2.8 for the potential difference of our charged system reduces to

$$\Delta V = k_e \sigma_1 \left[\Gamma_1 + \frac{A_1}{A_2} \Gamma_2 \right]$$

(2.2.10)

where

$$\Gamma_n = \iint_{D_n} \left\{ \frac{1}{[(x-x_0)^2 + (y-y_0)^2]^{\frac{1}{2}}} - \frac{1}{[(x-x_0)^2 + (y-y_0)^2 + z_0{}^2]^{\frac{1}{2}}} \right\} dy dx$$

From the definition of capacitance C, Equation 2.1.1, we finally obtain the capacitance of a flat parallel plate with dissimilar surface areas

$$C = \frac{Q}{|\Delta V|} = \frac{Q_1}{\left| k_e \frac{Q_1}{A_1} \left[\Gamma_1 + \frac{A_1}{A_2} \Gamma_2 \right] \right|} = \frac{A_1}{k_e \left[\Gamma_1 + \frac{A_1}{A_2} \Gamma_2 \right]}$$

$$C = \frac{A_1}{k_e \left[\Gamma_1 + \frac{A_1}{A_2} \Gamma_2 \right]} \tag{2.2.11}$$

An explicit capacitance value may be obtained for a square capacitor with asymmetrical surface areas given by $L_1{}^2$ and $L_2{}^2$. Let us compute the capacitance of such configuration. For computational convenience, let us evaluate the integral I given by Equation 2.2.12, which, in turn, would allow us to obtain explicit solutions for Γ_1 and Γ_2, and ultimately determine the capacitance of our configuration.

$$I = \int_{-L/2}^{L/2} \int_{-L/2}^{L/2} \frac{1}{(x^2 + y^2 + z_0{}^2)^{\frac{1}{2}}} dy dx \tag{2.2.12}$$

Using symmetrical arguments, it can be shown that the integral I is equivalent to

$$I = 8 \int_0^{\frac{\pi}{4}} \int_0^{\frac{l}{2\cos\theta}} \frac{1}{(r^2 + z_0{}^2)^{\frac{1}{2}}} r dr d\theta$$

$$I = 8z_0 \int_0^{\frac{\pi}{4}} \left\{ \frac{L}{2z_0\cos\theta} \left[1 + \left(\frac{2z_0}{L}\cos\theta \right)^2 \right]^{\frac{1}{2}} - 1 \right\} d\theta \tag{2.2.13}$$

By definition $L \gg z_0$, so that $(\frac{2z_0}{L}\cos\theta)^2 < 1$. Therefore, we may use the Binomial Theorem to expand the expression in square brackets to first order, which results in

$$I \approx 8z_0 \int_0^{\frac{\pi}{4}} \left\{ \frac{L}{2z_0\cos\theta} \left[1 + \frac{1}{2}\left(\frac{2z_0}{L}\cos\theta \right)^2 \right] - 1 \right\} d\theta$$

17

$$I \approx 8 \left[\frac{L}{2} \ln(\sqrt{2} + 1) + \frac{z_0^2}{L} \frac{\sqrt{2}}{2} - z_0 \frac{\pi}{4} \right] \tag{2.2.14}$$

We are now in the position to evaluate Γ_1 and Γ_2, provided we take the potential difference at the center ($x_0 = y_0 = 0$) of the square plates of sides L_1 and L_2. Doing so results in the following Γ values

$$\Gamma_1 = 8 \left[z_0 \frac{\pi}{4} - \frac{z_0^2}{L_1} \frac{\sqrt{2}}{2} \right] \quad \& \quad \Gamma_2 = 8 \left[z_0 \frac{\pi}{4} - \frac{z_0^2}{L_2} \frac{\sqrt{2}}{2} \right] \tag{2.2.15}$$

Substituting the Γ values of 2.2.15 into Equation 2.2.11, we obtain the capacitance C of an asymmetrical parallel plate capacitor with surface areas given by $A_1 = L_1{}^2$ and $A_2 = L_2{}^2$

$$C = \frac{A_1}{k_e \left[\Gamma_1 + \frac{A_1}{A_2} \Gamma_2 \right]}$$

$$C = \frac{L_1^2}{8k_e \left(z_0 \frac{\pi}{4} - \frac{z_0^2}{L_2} \frac{\sqrt{2}}{2} \right) \left[1 + \left(\frac{L_1}{L_2} \right)^2 \right]} \tag{2.2.16}$$

For a capacitor with equal surface area and neglecting the second term in the parenthesis (this assumption is valid since $z_0 \ll L$), Equation 2.2.16 reduces to the classical capacitance for a parallel-plate capacitor (Equation 2.1.6)

$$C = \frac{L_1^2}{16 \left(\frac{1}{4\pi\epsilon} \right) \left(z_0 \frac{\pi}{4} \right)} = \frac{\epsilon A_1}{z_0} \tag{2.2.17}$$

2.3 Deformation Theory

In this section, we present relevant concepts from *The Theory of Elasticity* by Lev Davidovich Landau and Evgeny M Mikhailovich Lifshitz [13] to illustrate key terminology. The reader familiar with basic deformation theory may omit this section and jump to section 2.4 without loss of generality.

2.3.1 The Strain Tensor

The displacement of a point due to the deformation is given by the *displacement vector* $\boldsymbol{u}$

$$\boldsymbol{u} = \boldsymbol{r'} - \boldsymbol{r} = \langle x_1' - x_1, x_2' - x_2, x_3' - x_3 \rangle \tag{2.3.1}$$

Or, equivalently,

$$u_i = x_i' - x_i$$

Consider two points that are close together, then the distance squared between the points, using Einstein's summation convention, is given by

$$dl^2 = dx_1^2 + dx_2^2 + dx_3^2 = dx_i^2 \tag{2.3.2}$$

$$dl'^2 = dx_1'^2 + dx_2'^2 + dx_3'^2 = dx_i'^2 = (dx_i + du_i)^2 \tag{2.3.3}$$

with Equation 2.3.2 before deformation and Equation 2.3.3 after deformation. But $du_i = \left(\frac{\partial u_i}{\partial x_k}\right) dx_k$, so the distance after the deformation dl' becomes

$$dl'^2 = dl^2 + 2u_{ik}dx_i dx_k \tag{2.3.4}$$

where u_{ik} is the *strain tensor* and is given by

$$u_{ik} = \frac{1}{2}\left(\frac{\partial u_i}{\partial x_k} + \frac{\partial u_k}{\partial x_i} + \frac{\partial u_l}{\partial x_i}\frac{\partial u_l}{\partial x_k}\right) \qquad (2.3.5)$$

Note that all indices (i, k and l) run from 1 to 3 so interchanges are permissible without affecting any summation. We also note that the strain tensor u_{ik} is symmetrical ($u_{ik} = u_{ki}$) and can be diagonalized. That is, only the diagonal components (u_{11}, u_{22}, and u_{33}) of the strain tensor are different from zero. If the strain tensor is diagonalized, then dl'^2 becomes

$$dl'^2 = (\delta_{ik} + 2u_{ik})dx_i dx_k$$

$$dl'^2 = \left(1 + 2u^{(1)}\right)dx_1^2 + \left(1 + 2u^{(2)}\right)dx_2^2 + \left(1 + 2u^{(3)}\right)dx_3^2 \qquad (2.3.6)$$

where δ_{ik} is the Kronecker delta function and $u^{(i)} = u_{ii}$. Along the ith principal axis, then

$$dx_i' = \left(1 + 2u^{(i)}\right)^{1/2}dx_i \quad \rightarrow \quad \frac{dx_i'}{dx_i} - 1 = \frac{dx_i'}{dx_i} - \frac{dx_i}{dx_i} = \frac{(dx_i' - dx_i)}{dx_i}$$

where $\frac{(dx_i' - dx_i)}{dx_i}$ is the relative extension along the ith principal axis. Using Equation 2.3.6 for dl'^2 and ignoring second order terms in the appropriate Taylor Series expansion, we find that

$$\frac{(dx_i' - dx_i)}{dx_i} = \left(1 + 2u^{(i)}\right)^{\frac{1}{2}} - 1 \approx \left(1 + \frac{1}{2}\left(2u^{(i)}\right)\right) - 1 \approx u^{(i)} \qquad (2.3.7)$$

From Equation 2.3.7, we can clearly see that when the relative extensions are small compared with unity, the strains are small. As a consequence, the third term in parenthesis of Eq. 2.3.5 is in the second order of smallness and we may be ignore it. Therefore, for small deformations, the strain tensor takes the following form

$$u_{ik} = \frac{1}{2}\left(\frac{\partial u_i}{\partial x_k} + \frac{\partial u_k}{\partial x_i}\right)$$
(2.3.8)

2.3.2 The Stress Tensor

When a deformation occurs, the arrangement of the molecules is changed, and the body ceases to be in its original state of equilibrium. Forces therefor arise which tend to return the body to equilibrium. These internal forces which occur when a body is deformed are called internal stresses. In the theory of elasticity, these forces are near-action forces, which act from any point only to neighboring points. Hence it follows that the forces exerted on any part of the body by surrounding parts act only the surface of this part. This assertion is not valid when the deformation of the body results in macroscopic electric fields in it, such as pyroelectric and piezoelectric bodies.

Let us consider the total force on some portion of the body:

$$\int F dV$$
(2.3.9)

where F is the force per unit volume. However, from the above assertion, the resultant force can be represented as the sum of the forces acting on all the surface elements. That is, for any portion of the body, each of the three components of the resultant of all the internal stresses can be transformed into an integral over a surface if we recognize that the vector F_i must be the divergence of a tensor of rank two, e.g. $F_i = \frac{\partial \sigma_{ik}}{\partial x_{ik}}$. Then,

$$\int F dV = \int F_i dV = \int \frac{\partial \sigma_{ik}}{\partial x_{ik}} dV = \oint \sigma_{ik}\, df_k$$
(2.3.10)

21

where σ_{ik} is the *stress tensor*.

Let us find the relationship between the stress tensor σ_{ik} in terms of the strain tensor u_{ik} for an isotropic body. We know that the deformation can be represented as the sum of a pure shear and a hydrostatic compression:

$$u_{ik} = \left(u_{ik} - \frac{1}{3}\delta_{ik}u_{ll}\right) + \frac{1}{3}\delta_{ik}u_{ll} \qquad (2.3.11)$$

where the first term in parenthesis is the shear component with the off-diagonal elements and the second term corresponds to hydrostatic compression. The free energy $\mathcal{F}$ of a deformed isotropic body is given by

$$\mathcal{F} = \mu(u_{ik} - \frac{1}{3}\delta_{ik}u_{ll})^2 + \frac{1}{2}Ku_{ll}{}^2 \qquad (2.3.12)$$

where μ is the *shear modulus* or *modulus of rigidity* and K is the *bulk modulus* or *modulus of hydrostatic compression*. Computing the total differential of the above equation while holding the temperature constant, we obtain

$$d\mathcal{F} = Ku_{ll}du_{ll} + 2\mu\left(u_{ik} - \frac{1}{3}\delta_{ik}u_{ll}\right)\left[d\left(u_{ik} - \frac{1}{3}\delta_{ik}u_{ll}\right)\right]$$

$$d\mathcal{F} = \left[Ku_{ll}\delta_{ik} + 2\mu\left(u_{ik} - \frac{1}{3}\delta_{ik}u_{ll}\right)\right]du_{ik}$$

$$d\mathcal{F} = \left[Ku_{ll}\delta_{ik} + 2\mu\left(u_{ik} - \frac{1}{3}\delta_{ik}u_{ll}\right)\right]du_{ik}$$

Dividing both sides by du_{ik} and evoking the relationship $\sigma_{ik} = \left(\frac{\partial F}{\partial u_{ik}}\right)_T$ from the Thermodynamics

of Deformation (see [12] for derivation), we finally obtain the desired relationship for the stress

tensor σ_{ik} in terms of strain tensor u_{ik} for an isotropic body:

$$\sigma_{ik} = \left(\frac{\partial F}{\partial u_{ik}}\right)_T = Ku_{ll}\delta_{ik} + 2\mu\left(u_{ik} - \frac{1}{3}\delta_{ik}u_{ll}\right) \tag{2.3.13}$$

where the subscript T refers to the fact that the strain tensor is measured at constant temperature.

For our purposes, we always assume the temperature to be fixed at room temperature. Sometimes,

it might be useful to express the strain tensor in terms of the stress tensor. To do so, let us proceed

as follows

1. Sum σ_{ii} of the diagonal terms for *hydrostatic compression*:

    $\sigma_{ii} = \sigma_{11} + \sigma_{22} + \sigma_{33}$

    substitute each term in the Equation 2.3.13 for stress tensor, then

    $\sigma_{ii} = Ku_{ll} + Ku_{ll} + Ku_{ll} = 3Ku_{ll}$

    $$\sigma_{ii} = 3K\begin{pmatrix} u_{11} & u_{12} & u_{13} \\ u_{21} & u_{22} & u_{23} \\ u_{31} & u_{32} & u_{33} \end{pmatrix} = 3K\begin{pmatrix} u_{11} & 0 & 0 \\ 0 & u_{22} & 0 \\ 0 & 0 & u_{33} \end{pmatrix} = 3Ku_{ii} \tag{2.3.14}$$

2. Plugging $\sigma_{ii} = 3Ku_{ii}$ into Equation 2.3.13 for stress tensor and noting that $\sigma_{ii} = \sigma_{ll}\delta_{ik}$

    $$\sigma_{ik} = K\left(\frac{1}{3}\sigma_{ll}\delta_{ik}\right) + 2\mu\left(u_{ik} - \frac{1}{3}\left(\frac{1}{3}\sigma_{ll}\delta_{ik}\right)\right)$$

    solving for u_{ik}, we finally obtain the strain tensor in terms of stress tensor for an isotropic

    body

$$u_{ik} = \frac{1}{9K}\sigma_{ll}\delta_{ik} + \frac{1}{2\mu}\left(\sigma_{ik} - \frac{1}{3}\sigma_{ll}\delta_{ik}\right) \qquad (2.3.15)$$

From the above equation, we see that for *small* deformations u_{ik} is proportional to applied forces σ_{ik}, e.g. Hook's. Now let us define some parameters that are typically found in literature and help us redefine the expressions for stress and strain tensors. The first of these parameters is the *Poisson's ratio* v, which is defined as the ratio of the transverse compression (u_{xx} or u_{yy}) to the longitudinal extension:

$$v = -\frac{u_{xx}}{u_{zz}}, \qquad \left(-1 \le v \le \frac{1}{2}\right) \qquad (2.3.16)$$

and the *modulus of extension* or *Young's modulus E* given by

$$\frac{1}{E} = \frac{1}{3}\left(\frac{1}{3K} + \frac{1}{\mu}\right) \qquad (2.3.17)$$

given the definitions of E and v, the expressions for the stress and strain tensors become

$$\sigma_{ik} = \frac{E}{(1+v)}\left[u_{ik} + \frac{v}{(1-2v)}u_{ll}\delta_{ik}\right] \qquad (2.3.18)$$

$$u_{ik} = \frac{1}{E}[(1+v)\sigma_{ik} - v\sigma_{ll}\delta_{ik}] \qquad (2.3.19)$$

It can be shown that for an elastic isotropic material, the following relationships hold for E, v, and G (shear modulus or modulus of rigidity)

$$E = 2(1+v)G, \qquad G = \frac{E}{2(1+v)}, \qquad v = \frac{E}{2G} - 1$$

2.3.3 Deformation of an Elastic Medium Occupying Half-space

In this section, we consider an elastic medium occupying a half-space (bounded on one side by an infinite plane) and attempt to determine the deformation of the medium caused by forces applied to its free surface. *The only constraint on the distribution of forces is that they must vanish at infinity in such a way that there is no deformation at infinity.* We take the free surface of the elastic medium as the xy-plane and the medium in $z > 0$. The final results for the displacement of points is given by displacement vector $\boldsymbol{u}$

$$\boldsymbol{u} = \langle u_x, u_y, u_z \rangle \tag{2.3.20}$$

where

$$u_x = \frac{(1+v)}{2\pi E} \left\{ \left[\frac{xz}{r^3} - \frac{(1-2v)x}{r(r+z)} \right] F_z + \frac{2(1-v)r + z}{r(r+z)} F_x + \frac{[2r(vr+z) + z^2]x}{r^3(r+z)^2} \left(xF_x + yF_y \right) \right\}$$

$$u_y = \frac{(1+v)}{2\pi E} \left\{ \left[\frac{yz}{r^3} - \frac{(1-2v)y}{r(r+z)} \right] F_z + \frac{2(1-v)r + z}{r(r+z)} F_y + \frac{[2r(vr+z) + z^2]y}{r^3(r+z)^2} \left(xF_x + yF_y \right) \right\}$$

$$u_z = \frac{(1+v)}{2\pi E} \left\{ \left[\frac{2(1-v)}{r} + \frac{z^2}{r^3} \right] F_z + \left[\frac{(1-2v)}{r(r+z)} + \frac{z}{r^3} \right] \left(xF_x + yF_y \right) \right\}$$

and $r^2 = x^2 + y^2 + z^2$.

Of particular interest are the displacement of points on the surface of the medium, which is given by plugging $z = 0$ into the set of Equations 2.3.20. For illustrative purposes, we have plotted the displacements of points in the z-direction, e.g. u_z from Eq. 2.3.20, in Figure 2.3.1.1 for $z = 0.4$ m, $E = 750$ kPa, $v = 0.49$, $F_z = F_x = F_y = 10$ N.

Figure 2.3.1.1 (a) The displacement of points u_z is more pronounced near the origin and quickly approaches zero. This is perhaps more evident if we inspect the contour plot shown in (b). For $-\frac{1}{2} \lesssim x, y \lesssim \frac{1}{2}$, we observe that u_z has already dropped by more than 80% of the maximum displacement.
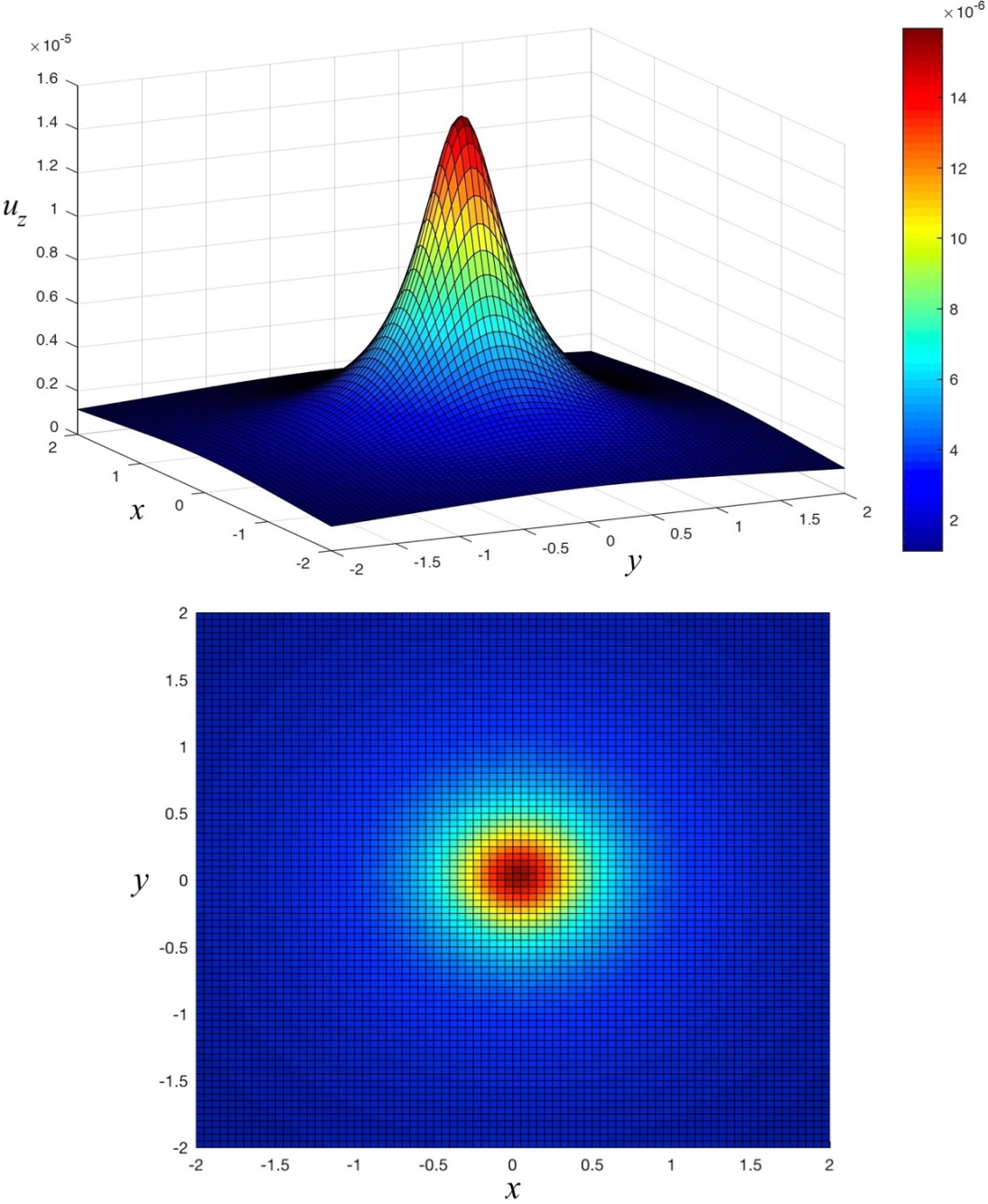
2.4 Capacitance of a Parallel Plate Capacitor after Deformation

In this section, we embark on the task to determine the capacitance of an original parallel plate capacitor *after* deformation as a result of external forces being applied to the surface area of the top plate. We assume that the bottom plate does not go through any deformation as a result of forces being applied to the top plate. This is reasonable assumption since the bottom electrode's thickness is small compared to the insulator's and can be thought of as being attached to a fixed surface unable to deform. Now, if we assume a *uniform compression* in the downward direction, then we would only need to consider deformations in the z-direction. This is because an infinitesimal *decrement* in the distance between the plates caused by a force results in a higher increment in capacitance than an infinitesimal *increment* of the surface area by the same force after deformation. Perhaps, this last statement would be more evident if we evoke the parallel plate approximation ($C \sim A/d$) and assume a *uniform compression* in the downward direction so that the area *A* remains approximately constant. Then, upon compression, the capacitance of the charged system becomes

$$C \sim \frac{A + \Delta A}{d - \Delta d} \tag{2.4.1}$$

From Equation 2.4.1, we can clearly see that since ΔA is negligible, the capacitance is dominated by the change of compression in the downward direction, e.g. Δd. For most practical applications, a uniform compression is hard, if not impossible, to achieve in practice. Even if a uniform normal force were to be applied to the top surface of a deformable capacitor, the amount of compression at each point on the capacitor's surface would not be the same. In effect, upon application of a uniform normal force, we would expect more deformation at sides of the capacitor as these can freely move outward. For the regions near the center of the capacitor, on the other

hand, the amount of deformation is less pronounced. This is because the atoms constituting the regions near the center cannot move freely sideways without colliding with nearby neighbor atoms. This is analogous to Fick's first law of diffusion which asserts that particles move from regions of higher concentration to lower concentration. In Chapter 4, we will show that this claim is consistent with our COMSOL Multiphysics simulations for our capacitive pressure sensor model. In the remaining of this section, we propose a mathematical procedure to calculate the capacitance of a capacitor after deformation.

We first let the initial top plate's surface be flat with surface charge density σ_1 and its surface be described by the function $g_1'(x, y) = z_0$. Similarly, we let the surface of the bottom plate be flat and described by $g_2'(x, y) = 0$ with surface charge density σ_2. Then, upon application of the force $\boldsymbol{F} = F_x \hat{\boldsymbol{x}} + F_y \hat{\boldsymbol{y}} + F_z \hat{\boldsymbol{z}}$ on the top plate ($\hat{\boldsymbol{x}}, \hat{\boldsymbol{y}}$, and $\hat{\boldsymbol{z}}$ are unit vector in the x, y, and z directions, respectively), its new surface becomes $g_1(x, y)$. The bottom plate's surface, on the other hand, is undeformed so that its new surface $g_2(x, y) = g_2'(x, y) = 0$. Then, using Equation 2.2.5, we find that the potential difference ΔV between the two plates *after* deformation becomes

$$\Delta V = V_+ - V_- = V[P_1(x_0, y_0, g_1)] - V[P_2(x_0, y_0, 0)] \tag{2.4.2}$$

where

$$V_+ = k_e \left[\iint_{D_1} \frac{\sqrt{1 + \left(\frac{\partial g_1}{\partial x}\right)^2 + \left(\frac{\partial g_1}{\partial y}\right)^2} \, \sigma_1 dy dx}{[(x - x_0)^2 + (y - y_0)^2]^{\frac{1}{2}}} + \iint_{D_2} \frac{\sigma_2 dy dx}{[(x - x_0)^2 + (y - y_0)^2 + g_1^2]^{\frac{1}{2}}} \right]$$

$$V_- = k_e \left[\iint_{D_1} \frac{\sqrt{1 + \left(\frac{\partial g_1}{\partial x}\right)^2 + \left(\frac{\partial g_1}{\partial y}\right)^2} \, \sigma_1 dy dx}{[(x-x_0)^2 + (y-y_0)^2 + g_1{}^2]^{\frac{1}{2}}} + \iint_{D_2} \frac{\sigma_2 dy dx}{[(x-x_0)^2 + (y-y_0)^2]^{\frac{1}{2}}} \right]$$

If we assume constant surface charge densities for both plates, then we may use the relation $\sigma_2 = -\sigma_1(A_1/A_2)$ from the set of Equations 2.2.9 to find the capacitance of the plates *after* deformation

$$C = \frac{A_1}{k_e \left[\Gamma_1 - \frac{A_1}{A_2} \Gamma_2 \right]} \tag{2.4.3}$$

where

$$\Gamma_1 = \iint_{D_1} \left[\frac{1}{[(x-x_0)^2 + (y-y_0)^2]^{\frac{1}{2}}} - \frac{1}{[(x-x_0)^2 + (y-y_0)^2 + g_1{}^2]^{\frac{1}{2}}} \right] \sqrt{1 + \left(\frac{\partial g_1}{\partial x}\right)^2 + \left(\frac{\partial g_1}{\partial y}\right)^2} \, dy dx$$

$$\Gamma_2 = \iint_{D_2} \left[\frac{1}{[(x-x_0)^2 + (y-y_0)^2 + g_1{}^2]^{\frac{1}{2}}} - \frac{1}{[(x-x_0)^2 + (y-y_0)^2]^{\frac{1}{2}}} \right] dy dx$$

Knowing how the top surface is deformed upon application of a force F, e.g. $g_1(x,y)$, allow us to obtain a numerical solution for the capacitance of the charged system. A much simpler expression than Equation 2.4.3 can be obtained if we make use of the parallel plate approximation. To this end, we first assume that we can subdivide the plates into smaller ones with area $\Delta A = \Delta x \Delta y$. We further assume that each pair of subdivision (one from the bottom plate and one from the top plate) is at the same potential so that all elements (capacitors) are in parallel. Then, the equivalent capacitance C_{eq} is

$$C_{eq} = C_1 + C_2 + \cdots + C_n = \sum_{i=1}^{n} C_i = \sum_{i=1}^{n} \frac{\epsilon \Delta A}{z_0 - g_1(x_i, y_i)}$$

$$C_{eq} = \lim_{n \to \infty} \sum_{i=1}^{n} \frac{\epsilon \Delta A}{z_0 - g_1(x_i, y_i)} = \int \frac{\epsilon dA}{z_0 - g_1(x, y)}$$

$$C_{eq} = \iint \frac{\epsilon dx dy}{z_0 - g_1(x, y)} \tag{2.4.4}$$

Again, knowing the surface $g_1(x, y)$ would allow us to determine the capacitance of the charged system. An unrealistic model but one for which we can readily obtain a numerical value for the capacitance from Equation 2.4.4 would be an elastic medium occupying half-space. To this end, we assume that the top plate's surface area has been deformed in such a way that its new surface g_1 could be approximated with a displacement function u_z of the insulating material. This is a reasonable assumption, since the insulating material thickness z_0 is typically much larger than the thickness of the top electrode's thickness. And, as a result, we would expect the top electrode's surface to go through the same amount of deformation as the top surface of the insulating material. Due to the big difference in thicknesses between these two materials, we could therefore approximate the displacement of points of the insulating material using Equation 2.3.20. Of particular interest is the displacement of points on the surface of the medium, which is obtained by substituting $z = 0$ for the z-component of the displacement vector $\boldsymbol{u}$. Doing so, results in

$$u_z(x, y) = \frac{(1 + v)}{2\pi E} \frac{1}{r} \left[2(1 - v)F_z + (1 - 2v)\frac{1}{r}\left(xF_x + yF_y\right) \right] \tag{2.4.5}$$

where $r^2 = x^2 + y^2$. Now, substituting Equation 2.4.5 into Equation 2.4.4 for $g_1(x, y)$, we obtain

$$C = \iint \frac{\epsilon dx dy}{z_0 - \frac{(1+v)}{2\pi E}\frac{1}{r}\left[2(1-v)F_z + (1-2v)\frac{1}{r}\left(xF_x + yF_y\right)\right]} \quad (2.4.6)$$

If the insulating material is Polydimethylsiloxane (PDMS), Equation 2.4.5 can be further simplified as the Poisson's ratio v is close to $1/2$ and $E = 750$ kPa. Inserting $v = 1/2$ into Equation 2.4.6, we obtain

$$C = \iint \frac{\epsilon dx dy}{z_0 - \frac{3F_z}{4\pi E}\frac{1}{r}} \quad (2.4.7)$$

We would like to point out that in deriving Equation 2.4.7, we are assuming that the deformations in the x and y directions are considered so small that the surface area remains approximately constant as the loads are applied. This is particularly true for small loads for which the relationship between strains and stresses is linear. Note also that the shear components of the force $\boldsymbol{F}$, F_x and F_y, have completely vanished, and, thus, have no effect on the theoretical value for the capacitance given by Equation 2.4.7. This result in quite surprising since this is precisely what we would expect upon application of purely shear force. Note that even the Poisson ratio v was not exactly $1/2$, the first term in square brackets of Equation 2.4.6 goes like $1/r$ whereas the second term (shear component) goes like $1/r^2$. Thus, the shear component of force vanishes faster as r increases and has little effect on the capacitance value. We can also readily see from Equation 2.4.7 that as the normal component of the force F_z increases, the plates are compressed more and more, and the capacitance increases. This effect is somewhat to be expected if we consider the

parallel plate approximation for which the capacitance increase as the distance between the plates decreases.

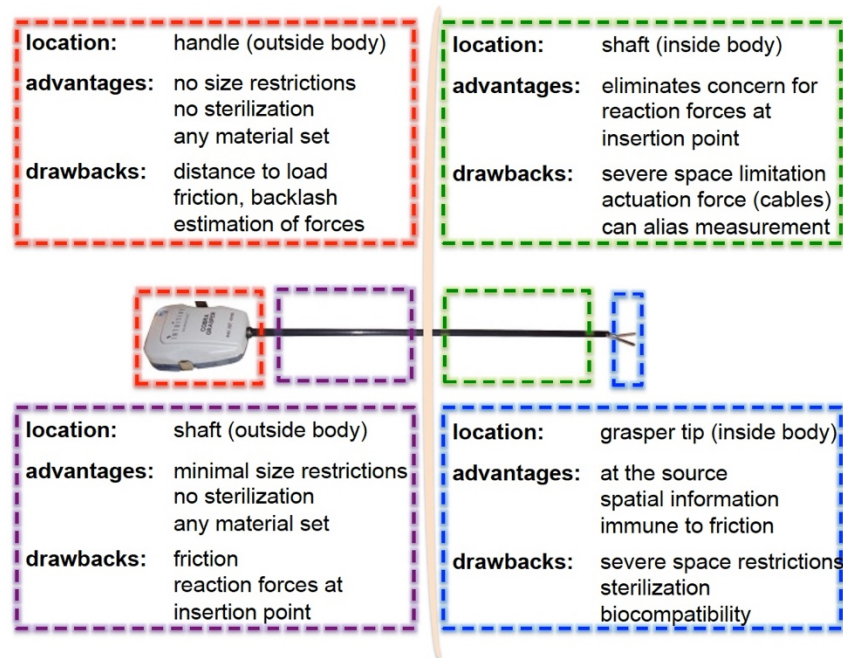**CHAPTER 3 SENSOR DESIGN AND WORKING PRINCIPLE**

In this chapter, we present previous work done by our research group. Our major goal here is to provide the reader with relevant information pertinent to our proposed sensor design and its working principle. The two aspects we highlight here concerning sensor design are the relevance of its location and its performance criteria, such as sensitivity and load dynamic range. The working principle, on the other hand, is of particular interest because explicit theoretical expressions for capacitive values are given and can be compared with the ones obtained from our COMSOL Multiphysics simulations. Since this chapter is essentially a summary, the reader is strongly encouraged to refer to pages 15-35 of reference [4] for a detailed description of this chapter.

3.1 Sensor Location and Performance Criteria

There are essentially four surgical grasper locations on which sensors can be integrated; each location with advantage and disadvantages as shown in Figure 3.1. Sensors integrated on the grasper tip, however, offer the most realistic representation of loads during surgery and have been proven to give accurate measurements during delicate surgical tasks, provide direct tissue-sensor interaction, and offer better spatial resolution. It was for these reasons that our proposed sensor was based on tip-integrated technologies, from which the capacitive modality was preferred. This preference was given due to its many advantages such as excellent sensitivity, large dynamic range, good spatial resolution, and controllable noise susceptibility. Two of these advantages, sensitivity

and dynamic range, are of particular interest since they are used as performance metrics required for detection of loads during surgical procedures for which dynamic range is 1 mN to 20 N, although loads exceeding about 14 N (285 kPa over a 56.4 mm^2 grasper area) result in tissue injury [14].

Fig. 3.1 Locations on the robotic grasper that have been identified as possible locations for sensor systems [4].

location:	handle (outside body)
advantages:	no size restrictions no sterilization any material set
drawbacks:	distance to load friction, backlash estimation of forces

location:	shaft (inside body)
advantages:	eliminates concern for reaction forces at insertion point
drawbacks:	severe space limitation actuation force (cables) can alias measurement

location:	shaft (outside body)
advantages:	minimal size restrictions no sterilization any material set
drawbacks:	friction reaction forces at insertion point

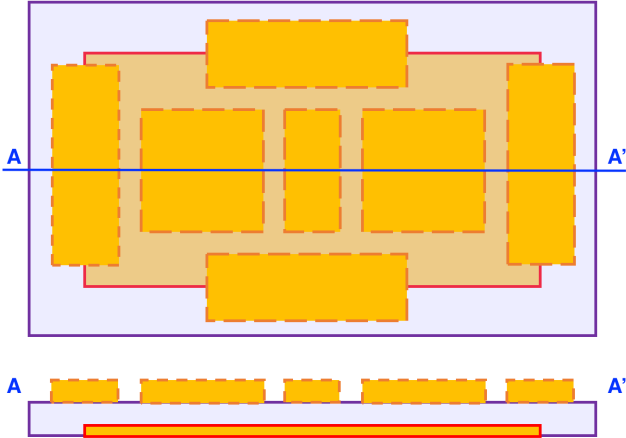| location:	grasper tip (inside body)
advantages:	at the source spatial information immune to friction
drawbacks:	severe space restrictions sterilization biocompatibility

3.2 Working Principle

Our proposed capacitive force sensor is designed in such a way that it would provide both normal and shear force data with high sensitivity for robotic surgical applications. The sensor is designed as a single-sided capacitive sensor for simpler integration with electronics and the surgical grasper. Furthermore, the design was motivated by the need to protect the sensor surface from sterilization and surgical environments while allowing for accurate measurements of the tissue-grasper interface [4]. The schematics of such design are shown in Fig. 3.2, while a top-view of the device along with a cross-sectional view are both displayed in Fig. 3.3. To aid in the

discussion of our sensor's working principle, we will constantly refer to the sensor layout shown

in Fig. 3.4, which highlights key parameters in the evaluation of capacitive values.

Fig. 3.2 Design of a multi-axis force sensor for haptic feedback system in robotic surgery. ■ Au gold, ☐ polydimethylsiloxane (PDMS), ■ substrate [4]. The material used for the electrodes was chosen to be gold because of its high electrical conductivity and its adhesiveness to PDMS, which was chosen as the insulator because of its stable flexibility, heat-restiveness, and insulating properties.
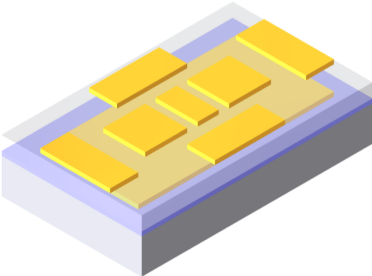
Fig. 3.3 Top and cross-sectional views of the proposed multi-axis force sensor. ■ top gold plate, ■ bottom gold plate, ■ PDMS. Adapted from [4].

Fig. 3.4 Capacitive values to be computed for the proposed multi-axis force sensor. Note that all the perimeter top electrodes (C_{in}'s) have the same area. Adapted from [4].

3.2.1 Compressive Sensor Theory

When a compressive normal force is applied to the proposed sensor, the signal is registered through the series combination of the two middle capacitors (C_{comp}), because the measurement is setup to be a *single-ended measurement*. That is, a measurement in which one of the compressive electrodes is used for the excitation while the other one is used for the response. Notice also from the cross-sectional view of Fig. 3.3 that the bottom gold electrode is common for both compressive electrodes so that when a single-ended measurement is made, the compressive electrodes (capacitors) act as a series combination. From circuit theory, we know that the equivalent capacitance C_{eq} for two capacitors (C_1 and C_2) in series is given by

$$C_{eq} = \frac{C_1 C_2}{C_1 + C_2} \tag{3.2.1}$$

35

Since the middle capacitors are identical, $C_{eq} = \frac{1}{2}C_1 = \frac{1}{2}C_{comp}$. Now, from the stress-strain

relation given by Eq. 2.3.19, $u_{ik} = \frac{1}{E}[(1+v)\sigma_{ik} - v\sigma_{ll}\delta_{ik}]$, we know that for a *linear elastic*

isotropic material $u_{ll} = \frac{1}{E}\sigma_{ll}$. In particular, for the z-component,

$$E = \frac{\sigma_z}{u_z} = \frac{F/A}{\Delta z/z_0} = \frac{F/A}{(z-z_0)/z_0} \tag{3.2.2}$$

Solving for z and substituting it into the parallel plate approximation, Eq. 2.2.17, we obtain

$$C = \frac{\epsilon A_{plate}}{\left(1 - \frac{F}{EA}\right)z_0} \tag{3.2.3}$$

Thus, using Eq. 3.24 we find that the equivalent capacitance as a function of applied (normal) force

for the compressive sensors is given by

$$C_{eq} = \frac{\epsilon s^2}{2z_0\left(1 - \frac{F}{EA}\right)} \tag{3.2.4}$$

Note that in deriving Eq. 3.2.3, we have assumed that that force will be equally distributed across

the top sensor surface area A_{comp} and that the amount of compression z is the same for all points

on A_{comp}. In chapter 4, we will verify the validity of these assumptions.

3.2.2 Shear Sensor Theory

When a shear force is applied x direction, the capacitance of the middle capacitors does not change, and the equivalent series capacitance between the positive (negative) input capacitance terminal $C_{in1(+)}$ $\left(C_{in1(-)}\right)$ and excitation terminal C_{exc} is found to be

$$C_{1,2} = \frac{\epsilon}{z}\left(\frac{A_{exc}A_{in1(\pm)}}{A_{exc} + A_{in1(\pm)}}\right) \tag{3.2.5}$$

where A_{exc} and $A_{in1(\pm)}$ are the overlap areas of the excitation and positive (negative) electrodes, respectively, and are defined by

$$\left.\begin{array}{l} A_{exc} = \dfrac{sl}{4} \\[2mm] A_{in1(\pm)} = \left(\dfrac{s}{4} \pm x\right)l \end{array}\right\} \tag{3.2.6}$$

Now, because the shear sensing electrodes are designed to make a differential measurement, *uniform compression* will not result in a registered shear measurement. One way to visualize this effect is to think about the following scenario: imagine the shear electrodes go through the same amount of compression, so the that C_1 and C_2 from Eq. 3.2.5 are exactly the same. Then, a differential capacitance measurement is $C = C_1 - C_2$ which is exactly equal to 0. If there is a shear component to the force, on the other hand, the differential capacitance in the x direction C_x becomes

$$C_x = C_1 - C_2$$

$$C_x = \frac{\epsilon A_{exc}^2}{z}\left[\frac{A_{in1(+)} - A_{in1(-)}}{\left(A_{exc} + A_{in1(+)}\right)\left(A_{exc} + A_{in1(-)}\right)}\right]$$

$$C_x = \frac{\epsilon}{2z}\left(\frac{s^2 lx}{s^2 - 4x^2}\right) \tag{3.2.7}$$

Following a similar argument and exploiting the symmetry of the sensor, we find that the differential capacitance due to a shear force in the y direction is given by

$$C_y = \frac{\epsilon}{2z}\left(\frac{s^2 ly}{s^2 - 4y^2}\right) \tag{3.2.8}$$

To find the change in capacitance due to an applied shear force, it is necessary to define a couple parameters first. The shear modulus G, which measures the resistance of solid to the motion of internal planes sliding past each other, is defined as the ratio of the shear stress τ to the shear strain γ and is given by Eq. 3.2.8. Fig. 4 illustrates the effect of a shear force F on a rectangular block.

$$G = \frac{\tau}{\gamma} = \frac{F/A}{\Delta x/z} \tag{3.2.9}$$

Fig. 3.5 A rectangular block under shear stress.
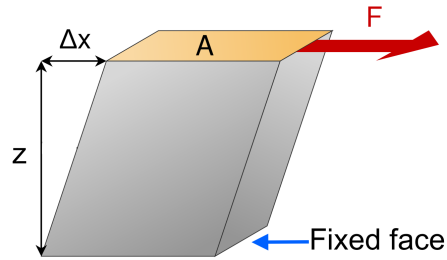
The shear modulus can also be expressed as follows:

$$G = \frac{E}{2(1+v)} \tag{3.2.10}$$

where E is the elastic modulus and v is the Poisson's ratio. Setting Eq. 3.2.9 and Eq. 3.2.10 equal to each other and solving for $\Delta x = x$, we obtain

$$x = \frac{2Fz(1+v)}{AE} \tag{2.3.11}$$

For a small displacement $\Delta x = x$, Eq. 3.2.7 can be further simplified to Eq. 2.3.12

$$C_x \approx \frac{\epsilon l x}{2z} \tag{3.2.12}$$

Finally, substituting Eq. 2.3.11 into Eq. 3.2.12, we obtain an expression that relates the capacitance to the applied shear force F:

$$C_x \approx \frac{\epsilon l(1+v)}{AE}F \tag{3.2.13}$$

Chapter 4 COMSOL Multiphysics Results

In this chapter, we present the capacitive values obtained from COMSOL Multiphysics for our micro-scale, tri-axial, capacitive-based, differential force sensor model shown in Figure 4.1 and commonly referred here as Capacitive Force Sensor (CFS). Special attention is given to the two idealities presented in section 3.3—uniform compression and the parallel plate approximation—

and how the introduction of these idealities makes the theoretical capacitive values deviate from the ones obtained from COMSOL Multiphysics. Our first efforts consist of various illustrations of how the CFS's surface is modified under compressive and shear loads. Recall from section 2.4 that knowing how the surface is deformed upon application of a force F allow us to obtain a numerical solution for the capacitance of a parallel plate *after* deformation. Thus, having a clear visualization of how the CFS's surface is deformed would allow us to decide what approximations can be made when computing the capacitance of a charged system. In the remaining of this chapter, we provide plots of the capacitance as function of applied force for our CFS model and some figures of merit such as sensitivity.

Fig. 4.1 Top view of our proposed capacitive force sensor (CFS), adapted from [4]. The parameters were chosen as follows: 40 nm gold electrode thickness; 50 μm insulator thickness z_0; 2.5 mm rectangle length l; 0.75 mm rectangle width $s/2$; and, 1.5 mm square side s.
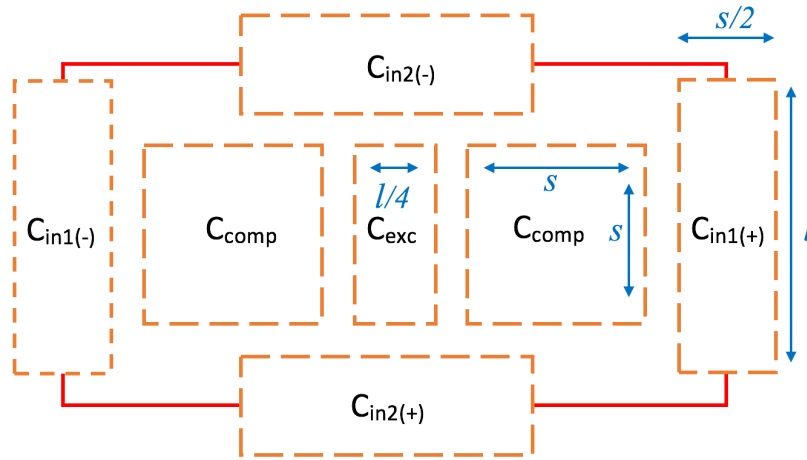

4.1 Sensor's Capacitance under Compressive Loads

The realized CFS model using COMSOL Multiphysics is illustrated in Figure 4.2. Please note that unless otherwise stated, we will be focusing on the corner shown in Figure 4.2 (b) for reasons that will become clear later on. Also, for clarifications purposes, the orientation of the xyz

coordinate axis will always be given on the bottom left corner of all the COMSOL Multiphysics figures. Having stressed these points, let us begin with our analysis of what happens when a *uniform compressive force* is applied on the top surface of our CFS model. As shown in Figure 4.3, as the load increases in magnitude, the points on the top surface go through larger and larger displacements whereas all the points on the bottom surface stay fixed. That the points on the bottom of the CFS stay fixed is to be expected, since it was chosen as fixed boundary condition.

Now, inspecting a top view of our CFS model, we notice that top edges of the CFS, particularly the corners, experienced the most deformation while the points near the *center* of the CFS are hardly deformed even for loads as large as 4 N as shown in Fig. 4.4. Notice also from the cross-sectional view of Fig. 4.4 that the amount of compression slowly increases from the center of the CFS towards the side, e.g. the xz-plane. We would expect, therefore, that the points near the center go through approximately the same amount of compression. The validity of the compressive capacitance given by Equation 3.2.3, which makes use of the parallel plate approximation, is confirmed, at least for our range of tested compressive loads.

Fig. 4.2 Realized CFS model using COMSOL. (a) A see-through diagram is shown here to appreciate the electrodes, particularly the bottom electrode which would otherwise not be visible. (b) Zoom-in of the corner that the blue arrow in (a) points to.
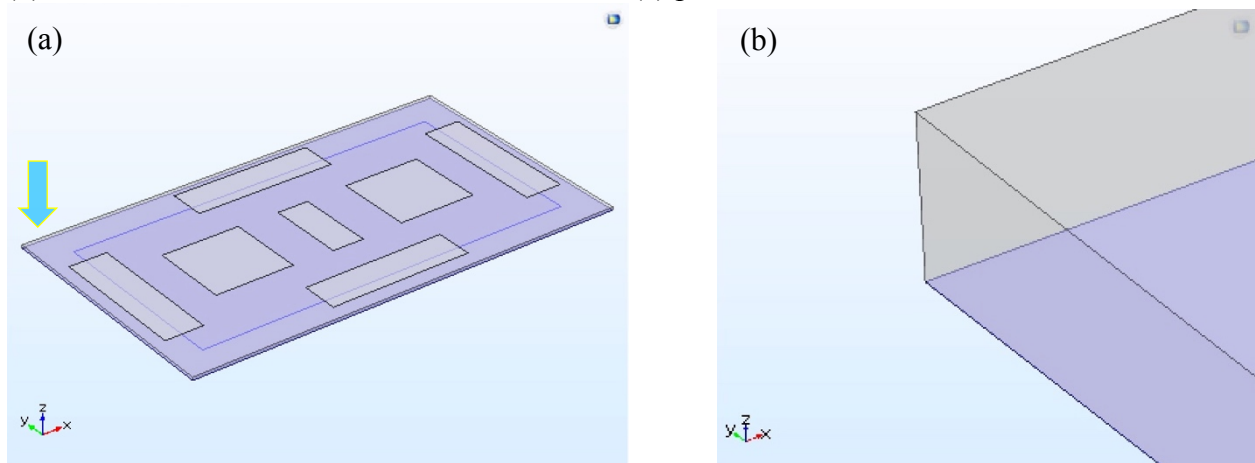
Fig. 4.3 Deformation of the CFS under various *uniform* compressive loads. Here, the amount of compression is given by F_z and is uniformly applied throughout the top of the CFS. The legend on the right-hand side shows the magnitude of the displacement.
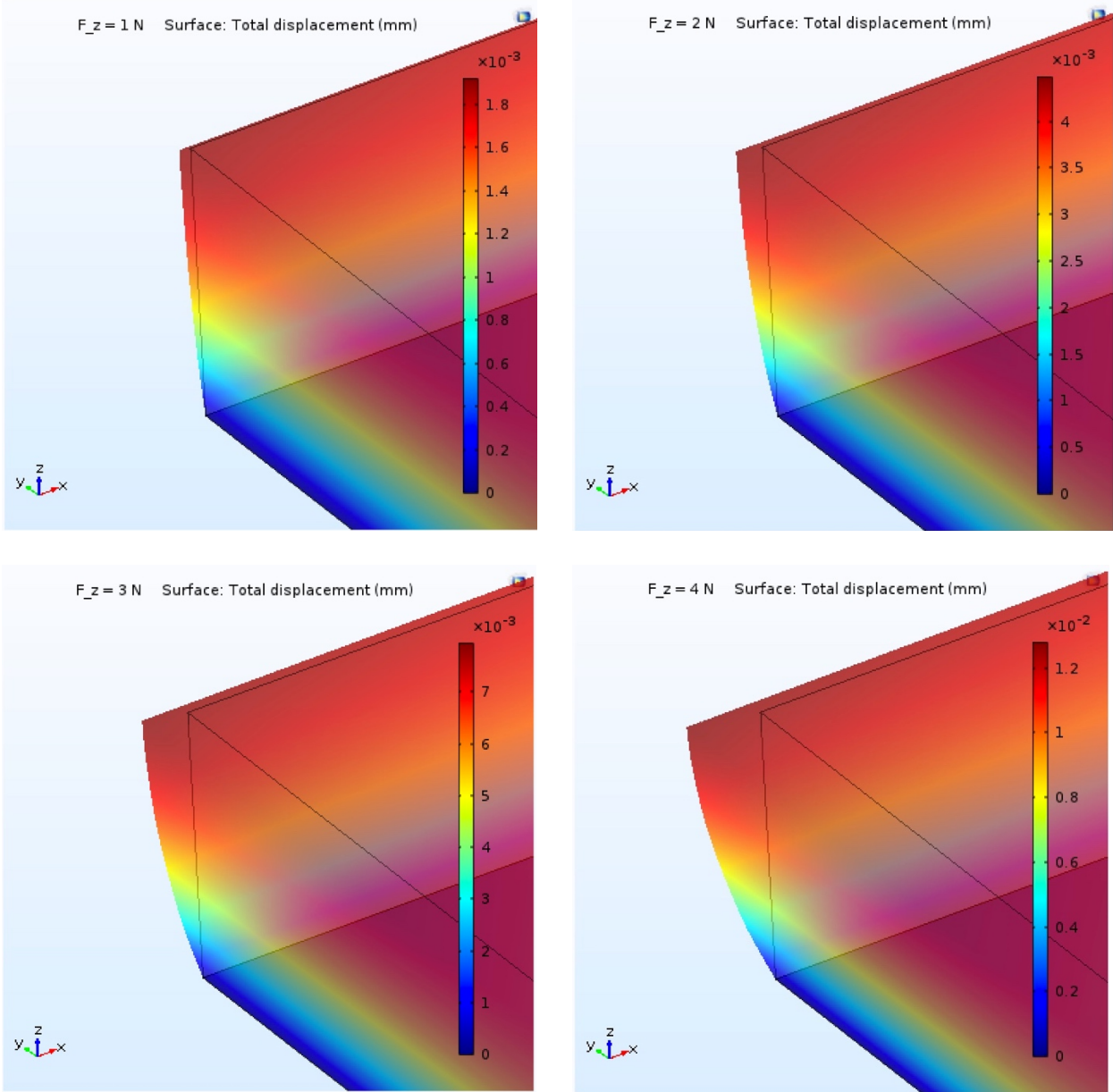
Fig. 4.4 Top and cross-sectional views of the CFS under a uniform compressive load of 4 N.
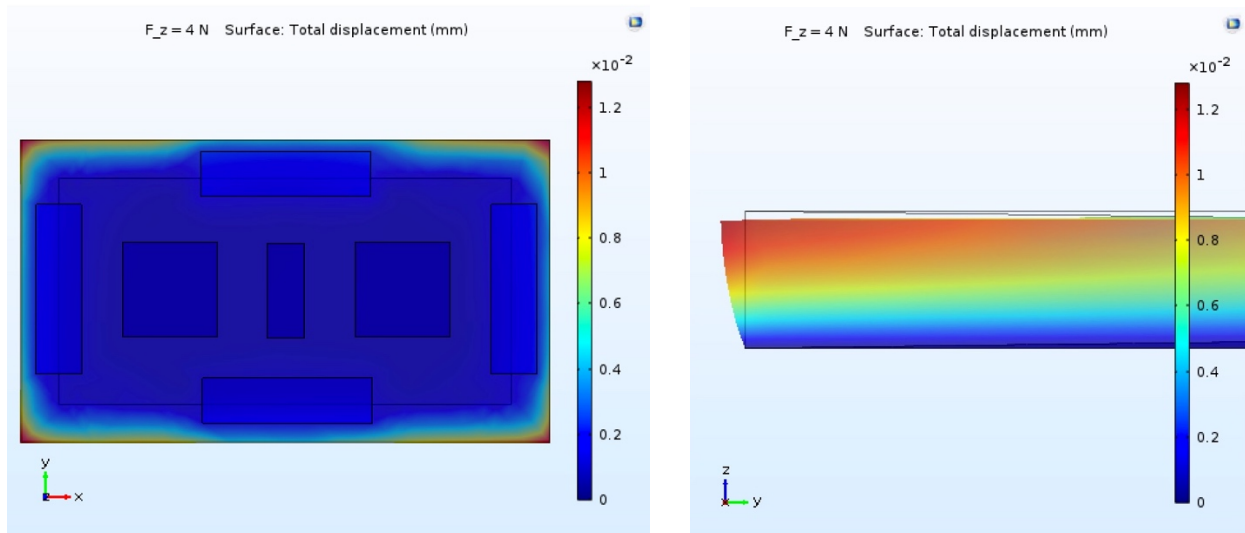

It is worth mentioning that Equation 3.2.3 is only for valid for $\frac{F}{EA} \ll 1$ and is, therefore, not much useful for our studies. We do have, however, experimental results for the normal capacitance as a function of applied force, shown in Fig. 4.5, which are in close agreement with the capacitive values obtained from COMSOL Multiphysics, shown in Fig. 4.6. Notice also the linearity of both plots from which the sensitivity, a figure of merit, can be obtained from the slope. The sensitivity for the experimental results is approximately 3 fF/N whereas that from COMSOL Multiphysics 0.7 fF/N.

Fig. 4.5 Experimental results for normal capacitance as a function of applied force [15].
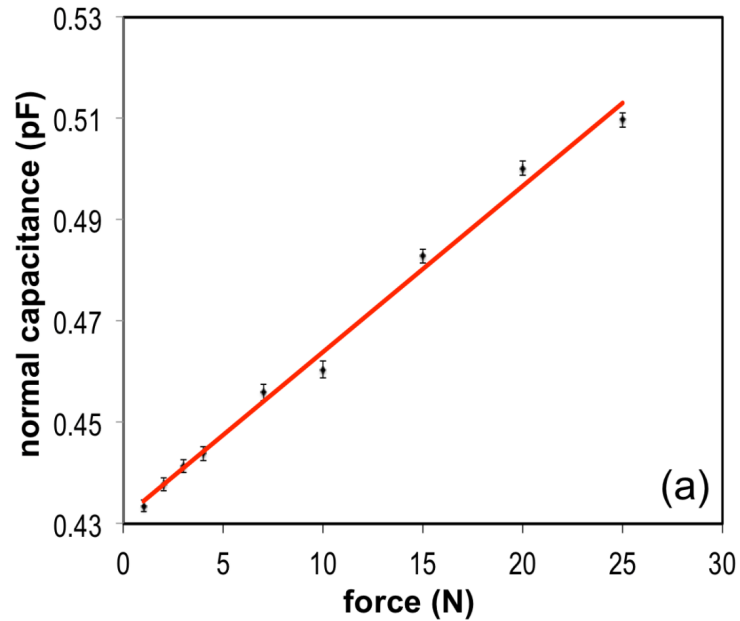
**Fig. 4.6** COMSOL results for normal capacitance as a function of applied force.
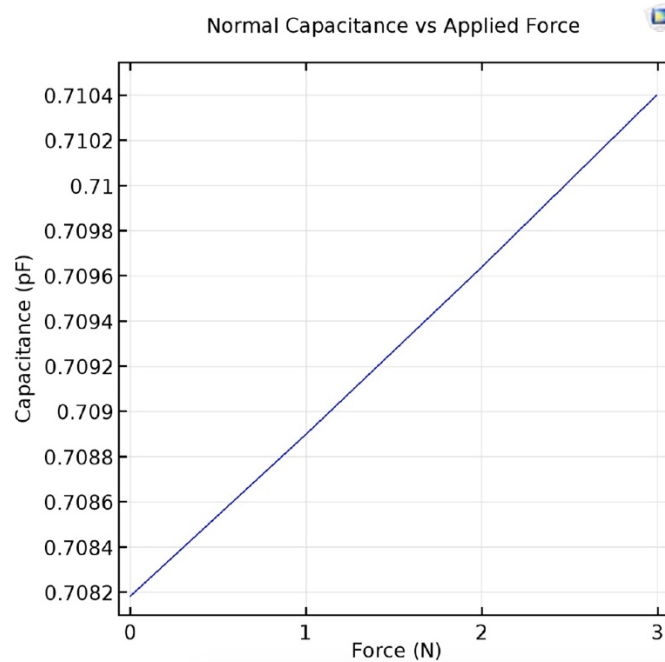
4.2 Sensor's Capacitance under Shear Loads

Our analysis for this section begins with the deformation effect of a shear load on the top surface of our CFS model. As shown in Figure 4.7, as the load increases in magnitude, the points

on the top surface go through larger and larger displacements whereas all the points on bottom surface stay fixed as this last surface was chosen as fixed boundary condition. We also notice that as the shear load increases, the thickness of the CFS, relative to the bottom surface, decreases. This effect is of particular interest, since even if a differential capacitive measurement was made, we would still have to account for this decrease in thickness. Recall from Eq. 3.2.5, $C_{1,2} = \frac{\epsilon}{z}\left(\frac{A_{exc}A_{in1(\pm)}}{A_{exc}+A_{in1(\pm)}}\right)$, that thickness z is *fixed*, when, if fact, it is being reduced as larger and larger shear loads are applied. We would, therefore, expect a higher capacitive value than the theoretical one for large loads.

Note also that this reduction in thickness would also have significant implications on the compressive capacitive values for *large* shear loads. The differential capacitance given by Equation 3.2.13 would therefore be valid only for small loads such that z remains approximately constant. In addition, we would also like to point out that since the shear electrodes are not completely aligned with the bottom electrode—some of the shear electrode's surface area lies outside of the bottom electrode when viewed from above—we would expect strong fringe field effects and, therefore, a non-linear relationship between shear capacitance and force. In fact, this is precisely what the COMSOL Multiphysics simulations predict as shown in Fig. 4.8.

Fig. 4.7 Deformation of the CFS under various shear loads. Here, the magnitude of the shear force is given by F_x and is applied on the top of the CFS. The legend on the right-hand side shows the magnitude of the displacement.
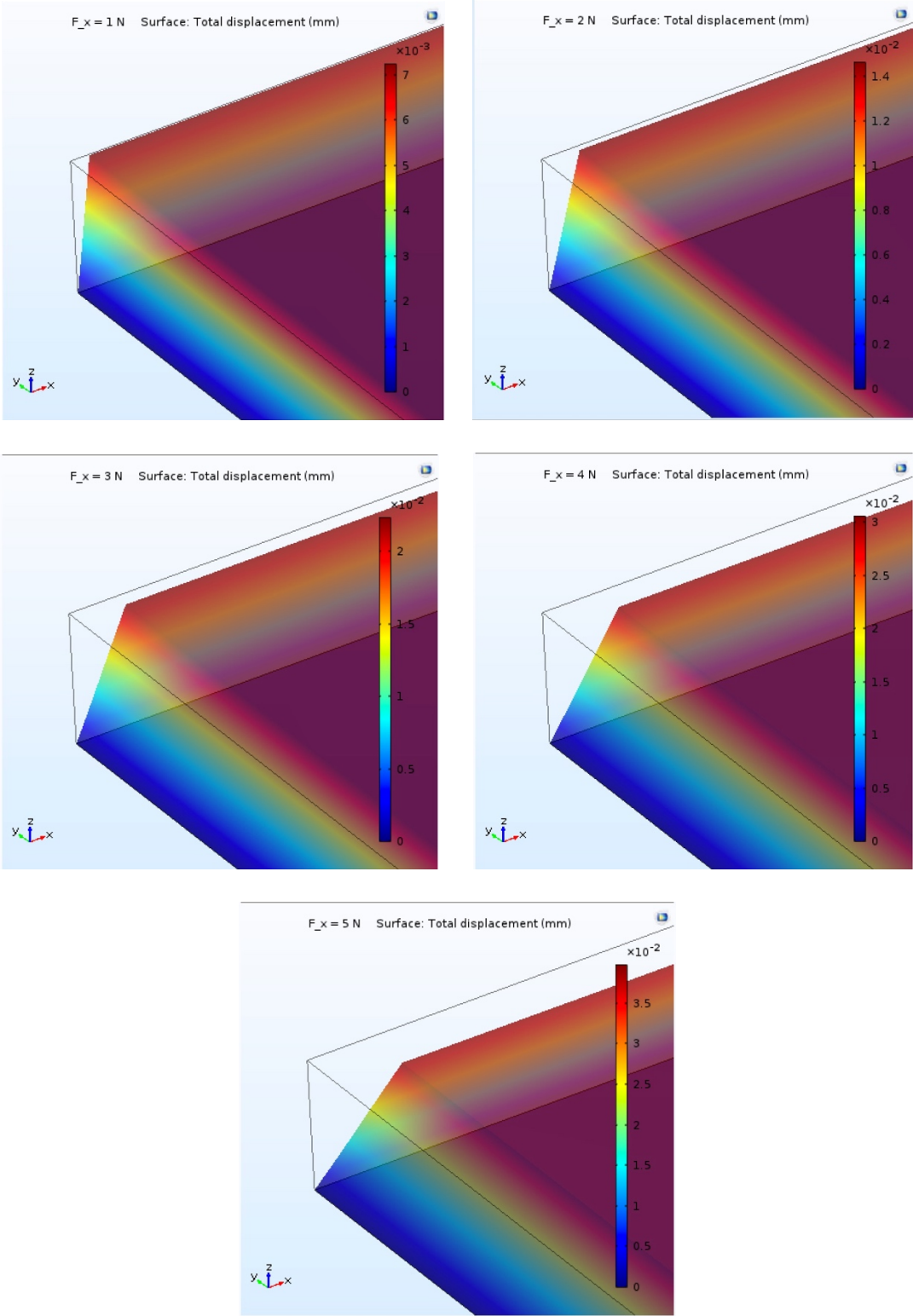
Fig. 4.8 Shear capacitance as a function of applied (shear) force in the positive x-direction for (a) the shear electrode $C_{in1(-)}$ and (b) the shear electrode $C_{in1(+)}$. Notice the capacitance for $C_{in1(-)}$ is slightly bigger than $C_{in1(+)}$ for all shear loads. This is because as the shear force in the positive x-direction increases, the overlapping area for $C_{in1(-)}$ increases while that for $C_{in1(+)}$ decreases. That the shear capacitance for $C_{in1(+)}$ continues to increase as the shear force increases is due to the decrease in thickness of the CFS. Note also the predicted non-linear relation between capacitance and shear force. It is worth mentioning that this relation also holds true for the differential capacitance shown in (c).

(a)

(b)

(c)
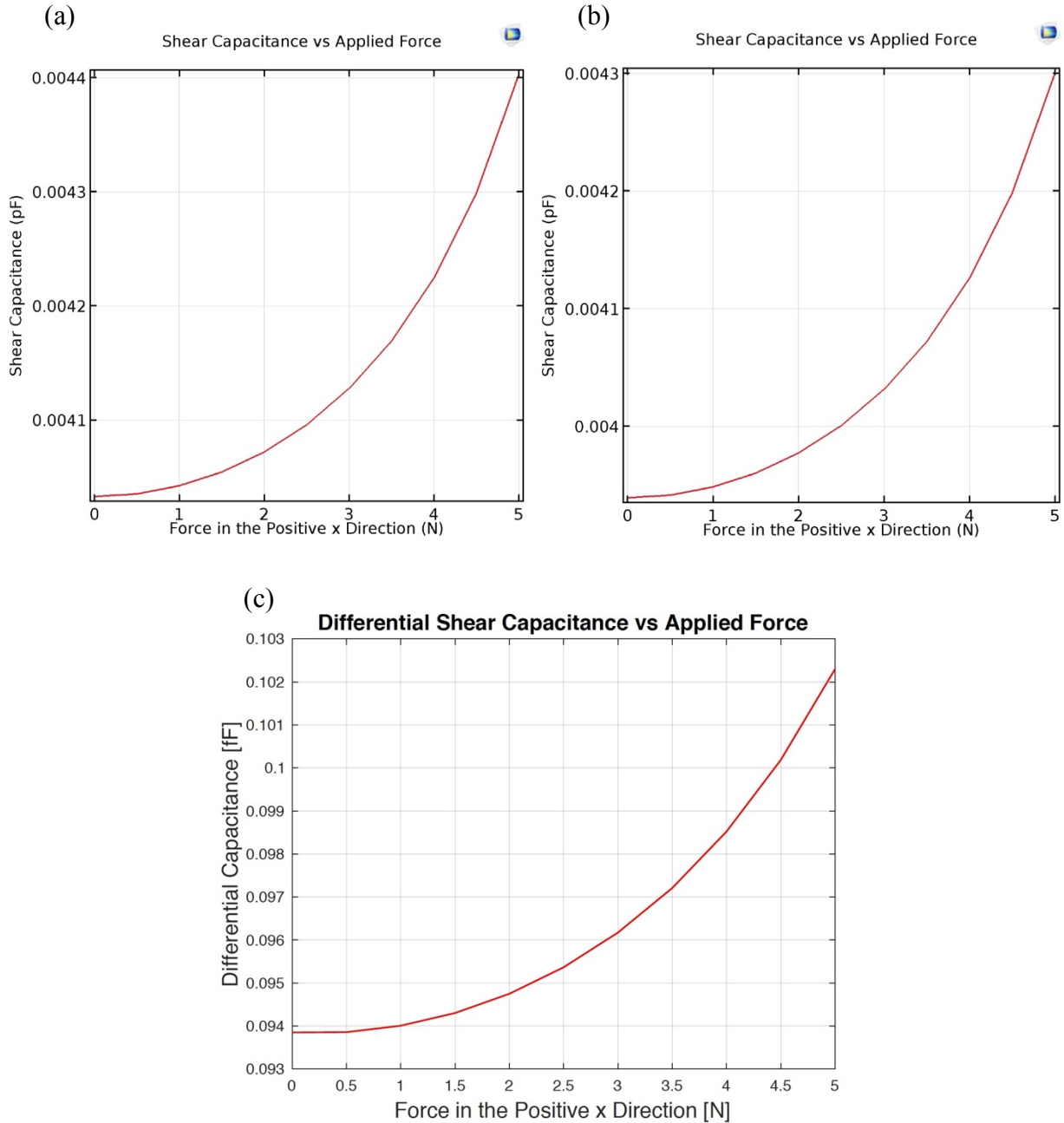
4.3 Summary and Conclusion

We have tested and confirmed the validity of some of the theoretical capacitance approximations for our capacitive force sensor. In general, it was found that for small applied loads, such that the relationship between stress and strain is linear, our approximations hold true. Given that the chosen insulating material, PDMS, exhibits a non-linear behavior between strain and stress, we anticipated that for large loads, our approximations would no longer remain valid as verified by our COMSOL Multiphysics simulations. This was particularly true for shear capacitances, without mentioning the fringe field effects, which would have to be taken into account for better capacitance estimates. We believe that knowing how the electrode's surface is deformed can yield more accurate capacitive values. This is because the gamma functions from section 2.4 can be directly evaluated to obtain a numerical solution for capacitance, assuming *only* a constant charge density. Current work is being done to optimize the sensitivity of our current capacitive force sensor model. And strongly believe that by adjusting the geometric parameters from our current capacitive force sensor model, we can achieve this without the need to fabricate the capacitive force sensor model again, but rather with the aid of COMSOL Multiphysics.

REFERENCES

1. History of Minimally Invasive Surgery. Shawn D. St. Peter and George W. Holcomb III.

2. N. C. f. H. Statistics, "National Hospital Discharge Survey: 2010 Table," 2010.

3. C. Tsui, R. Klein, and M. Garabrant, "Minimally invasive surgery: national trends in adoption and future directions for hospital strategy," Surg Endosc, vol. 27, pp. 2253-7, Jul 2013.

4. O. H. Paydar, "Tactile Sensors for Minimally Invasive Surgical Systems," 2016.

5. M. Kitagawa, A. M. Okamura, B. T. Bethea, V. L. Gott, and W. A. Baumgartner, "Analysis of Suture Manipulation Forces for Teleoperation with Force Feedback," in Medical Image Computing and Computer-Assisted Intervention — MICCAI 2002: 5th International Conference Tokyo, Japan, September 25–28, 2002 Proceedings, Part I, T. Dohi and R. Kikinis, Eds., ed Berlin, Heidelberg: Springer Berlin Heidelberg, 2002, pp. 155-162

6. Y. S. Kwoh, J. Hou, E. A. Jonckheere, and S. Hayati, "A robot with improved absolute positioning accuracy for CT guided stereotactic brain surgery," Biomedical Engineering, IEEE Transactions on, vol. 35, pp. 153-160, 1988.

7. Michael J. Mack, Minimally Invasive and Robotic Surgery. JAMA, February 7, 2001 — Vol 285, No. 5.

8. S. De, J. Rosen, A. Dagan, B. Hannaford, P. Swanson, and M. Sinanan, "Assessment of tissue damage due to mechanical stresses," International Journal of Robotics Research, vol. 26, pp. 1159-1171, Nov 2007.

9. C. J. Mohr, G. S. Nadzam, and M. J. Curet, "Totally robotic Roux-en-Y gastric bypass," Archives of Surgery, vol. 140, pp. 779-785, Aug 2005.

10. Gregory Tholey, Jaydev P. Desai, and Andres E. Castellanos. Force Feedback Plays a Significant Role in Minimally Invasive Surgery. January 2005.

11. http://www.uchospitals.edu/specialties/minisurgery/benefits/index.html

12. https://commons.wikimedia.org/wiki/File:VFPt_capacitor-thin-rods.svg

13. Theory of Elasticity. 3rd Edition. L. D. Landau and E. M. Lifshitz. Course of Theoretical Physics.

14. S. De, J. Rosen, A. Dagan, B. Hannaford, P. Swanson, and M. Sinanan, "Assessment of tissue damage due to mechanical stresses," *International Journal of Robotics Research*, vol. 26, pp. 1159-1171, Nov 2007.

15. Y. Dai, O. Paydar et. al. Miniature Multi-Axis Force Sensor for Haptic Feedback Systems in Robotic Surgery.